

Active learning of collinear magnetic Moment Tensor Potentials using the spin-MLIP package from soft-constrained spin-polarized DFT calculations: a case study of Fe-Pd

Arseniy Burov^a, Alexey S. Kotykhov^{a,b}, Dmitry A. Aksyonov^a, Ivan S. Novikov^{b,*}, Vladimir V. Ladygin^c

^aSkolkovo Institute of Science and Technology, Bolshoy boulevard 30, Moscow, 121205, Russian Federation

^bHSE University, Faculty of Computer Science, Pokrovsky boulevard 11, Moscow, 109028, Russian Federation

^cCalifornia Institute of Technology, Pasadena, California, 91125, United States of America

Abstract

Explicit incorporation of magnetic degrees of freedom in machine-learning interatomic potentials (magnetic MLIPs) plays a crucial role in the correct description of magnetic materials and their properties. An important ingredient for fitting of magnetic MLIPs is spin-polarized density functional theory (DFT) calculations with non-equilibrium magnetic moments, i.e. DFT calculations with constraints on magnetic moments. In this study, we present a workflow for active learning of magnetic Moment Tensor Potential (mMTP) during molecular dynamics (MD) simulations. Magnetic MTP and its active learning algorithm were implemented in the open-source spin-MLIP code, DFT soft-constrained spin-polarized calculations were performed with the VASP code, and MD simulations were conducted in the open-source LAMMPS code. We test our workflow on the Fe-Pd crystal. The dependencies of magnetization and density of states (DOSs) on the volume of a supercell (or, pressure) are in good agreement with those calculated with DFT. Furthermore, the calculated DOSs correspond to the experimental ones.

1. Introduction

An accurate description of magnetism plays an important role in the theoretical study of magnetic materials and their properties. Nowadays, machine-learning interatomic potentials (MLIPs) is a popular and widely-used tool for the theoretical investigation of materials. During the last five years, many MLIPs explicitly incorporating magnetic degrees of freedom (magnetic MLIPs) have been developed [1, 2, 3, 4, 5, 3, 6, 7, 8, 9, 10, 11, 12, 13, 14]. Magnetic MLIPs are typically trained on energies, forces, and stresses calculated with density functional theory, yield the accuracy of DFT calculations, and enable predicting magnetic properties of materials such as Curie temperature, Neel temperature, and magnetization, as well as vibrational and mechanical properties like phonon spectra, bulk modulus, and elastic constants for accurate prediction of which it is necessary to take magnetism into account in magnetic materials.

The main difficulty in the construction of magnetic MLIPs is the creation of a training set for their fitting. The first challenge here is the automated selection of the configurations to be added to a training set. As opposed to the non-magnetic case, here we also have magnetic moments as an additional degree of freedom and, therefore, it becomes even more difficult to create a training set manually by following only physical intuition. Furthermore, an algorithm for automated selection of configurations enables reducing a number of configurations in a training set, which is critical, as spin-polarized DFT calculations typically used to create a training set for magnetic MLIPs are even more time consuming than conventional (non-spin-polarized) DFT calculations. The second challenge is the need to have configurations with non-equilibrium (excited) magnetic moments in a training set, as they are explicitly included in a functional form of magnetic MLIPs along with atomic positions, types, and lattice vectors. Just as we require non-equilibrium atomic positions to properly fit non-magnetic MLIPs, we also need non-equilibrium magnetic

*isnovikov@hse.ru

moments to fit magnetic MLIPs. Due to the above reasons, it can be rather difficult for a user to implement a workflow that enables for automated training of magnetic MLIPs. Furthermore, to our knowledge, only the codes DeePSPIN [15] and mag-ace [16] include magnetic MLIPs and are open-source.

In this study, we describe a workflow for the automated construction of training sets to fit the magnetic MLIP during atomistic simulations — specifically, magnetic Moment Tensor Potential (magnetic MTP, or mMTP) proposed in [17] for multi-component magnetic materials and provide a workflow for its automated fitting. As an example of atomistic simulations, we consider molecular dynamics simulations. To select the configurations to be added to a training set, we use an active learning algorithm formulated in [18] and based on the maxvol algorithm [19]. To compute DFT energies, forces, and stresses for selected configurations, we utilize soft-constrained spin-polarized DFT calculations that enable approximately preserving non-equilibrium magnetic moments as a result of calculations. In addition to the algorithm for automated fitting of mMTP, we provide an open-source code called spin-MLIP in which mMTP and the algorithm for its active learning were implemented [20], its interface [21] with the LAMMPS code [22, 23], and the workflow [24] including scripts for molecular dynamics simulations with LAMMPS, for selection of configurations with spin-MLIP, for soft-constrained DFT calculations with the VASP code [25, 26], and for fitting of mMTP also using spin-MLIP. As an example of an atomic system, we take Fe-Pd and calculate the dependencies of its magnetization and density of states (DOSs) on the volume of a supercell (or, pressure) with the fitted mMTP. The mentioned dependencies calculated with mMTP are close to the DFT ones and DOSs obtained with mMTP are also close to the experimental data.

2. Methodology

2.1. Magnetic Moment Tensor Potential

We used magnetic Moment Tensor Potential (magnetic MTP, mMTP) as a machine-learning interatomic potential for magnetic materials. The mMTP model was first developed for single-component materials in [7] and is based on a non-magnetic version of MTP [27]. The functional form of the chosen potential explicitly depends on the magnitude of the scalar magnetic moments of the atoms, thus enabling the potential to describe collinear magnetism not only qualitatively but also quantitatively.

The mMTP model is local, i.e. the potential energy of a configuration is decomposed into the sum of the energies of each atomic environment \mathcal{N}_i :

$$E^{\text{mMTP}} = \sum_{i=1}^{N_{\text{atoms}}} V(\mathcal{N}_i), \quad (1)$$

where N_{atoms} is a number of atoms in a supercell and an atomic neighborhood \mathcal{N}_i is a set of atoms within a sphere of cutoff radius R_{cut} around the atom i . Each atomic neighborhood contains information about the distances $|\mathbf{r}_{ij}|$ between the central atom and its neighbors, as well as the atomic types z_i and z_j , and the magnetic moments m_i and m_j of central and neighboring atoms:

$$\mathcal{N}_i = \{(\mathbf{r}_{ij}, z_i, z_j, m_i, m_j), j = 1, \dots, N_{\text{nbh}}^i : |\mathbf{r}_{ij}| < R_{\text{cut}}\}. \quad (2)$$

The energy for each atomic environment is represented as a linear combination of basis functions B_α :

$$V(\mathcal{N}_i) = \sum_{\alpha} \xi_{\alpha} B_{\alpha}. \quad (3)$$

The coefficients ξ_{α} are trainable parameters. The basis functions are obtained as contractions of moment tensor descriptors $M_{\mu,\nu}$ yielding a scalar:

$$M_{\mu,\nu}(\mathcal{N}_i) = \sum_j f_{\mu}(|\mathbf{r}_{ij}|, z_i, z_j, m_i, m_j) \mathbf{r}_{ij}^{\otimes \nu}. \quad (4)$$

The function f_{μ} depends on the interatomic distances and magnetic moments of the particles for each pair of atomic types and forms the radial part. The outer product \otimes , taken ν times, represents the angular part of the moment

tensor descriptor. Thus, when ν is equal to zero, the angular part will be a scalar. When ν is equal to one, the angular part represents the initial vector of the interatomic distance, and when ν is equal to two, it will be a matrix.

The radial part of the moment tensor descriptor consists of various polynomials:

$$f_\mu(|\mathbf{r}_{ij}|, z_i, z_j, \mathbf{m}_i, \mathbf{m}_j) = \sum_{\zeta=1}^{N_\phi} \sum_{\beta=1}^{N_\psi} \sum_{\gamma=1}^{N_\psi} c_{\mu, z_i, z_j}^{\zeta, \beta, \gamma} \phi_\zeta(|\mathbf{r}_{ij}|) \psi_\beta(\mathbf{m}_i) \psi_\gamma(\mathbf{m}_j) (R_{\text{cut}} - |\mathbf{r}_{ij}|)^2. \quad (5)$$

The functions ϕ_ζ , ψ_β , and ψ_γ are Chebyshev polynomials of the first kind corresponding to the orders indicated by the subscript. Symbols N_ϕ and N_ψ denote the sizes of the radial and magnetic bases, respectively. The interatomic distance defined on the interval $(R_{\text{min}}, R_{\text{cut}})$ and the magnetic moments from the interval $(-M_{\text{max}}^{z_i}, M_{\text{max}}^{z_i})$ are mapped onto the interval $(-1, 1)$. Each type of atom z_i has its own maximum magnetic moment $M_{\text{max}}^{z_i}$ in the training set. The parameters $c_{\mu, z_i, z_j}^{\zeta, \beta, \gamma}$ are trainable. The inclusion of the functions ψ_β and ψ_γ is the main difference between mMTP and the original non-magnetic MTP. Because of this, the radial part of the mMTP contains N_ψ^2 times more parameters than the original MTP. Since the functions ψ_β and ψ_γ depend only on the magnitude of magnetic moments and the angular part does not include magnetic moments at all, mMTP can only describe collinear magnetism.

As an infinite number of contractions of moment tensor descriptors yielding a scalar can be constructed for different values of μ and ν , it is necessary to limit a number of contractions. Therefore, the concept of moment tensor descriptor level is introduced:

$$\text{lev} M_{\mu, \nu} = 2 + 4\mu + \nu. \quad (6)$$

The coefficients in (6) were empirically selected in [28]. The level of contraction of moments is defined as the sum of the levels of moments. For example, $\text{lev}(M_{0,0}^4) = 8$ and $\text{lev}(M_{0,1} \cdot M_{2,1}) = 14$. The concept of a potential level lev_{mMTP} is also introduced, representing the maximum permissible level of moment contractions. Thus, basis functions consist of all permitted moment contractions, i.e., whose level is lower than the potential level ($\text{lev} B_\alpha \leq \text{lev}_{\text{mMTP}}$).

Denote $\theta = \{\xi_\alpha, c_{\mu, z_i, z_j}^{\zeta, \beta, \gamma}\}$ by the set of all trainable parameters from equations (3) and (5). The symbols \mathbf{R} , \mathbf{Z} , \mathbf{M} , and \mathbf{L} denote the coordinates, types, and magnetic moments of atoms in a system, and lattice vectors, respectively. For physical reasons, the energy of the system should not change when the magnetic moments of all atoms are flipped. To satisfy this condition, the functional form of the potential is symmetrized:

$$E^{\text{mMTP}}(\theta) = \frac{E(\theta, \mathbf{R}, \mathbf{Z}, \mathbf{L}, \mathbf{M}) + E(\theta, \mathbf{R}, \mathbf{Z}, \mathbf{L}, -\mathbf{M})}{2}. \quad (7)$$

The optimal parameters of the potential are determined by minimizing the loss function:

$$\text{Loss}(\theta) = \sum_{k=1}^K \left[w_e \left(E_k^{\text{mMTP}}(\theta) - E_k^{\text{DFT}} \right)^2 + w_f \sum_{i=1}^{N_{\text{atoms}}} \left(\mathbf{f}_{i,k}^{\text{mMTP}}(\theta) - \mathbf{f}_{i,k}^{\text{DFT}} \right)^2 + w_s \sum_{a,b=1}^3 \left(\sigma_{ab,k}^{\text{mMTP}}(\theta) - \sigma_{ab,k}^{\text{DFT}} \right)^2 \right]. \quad (8)$$

Thus, the training set for the potential consists of configurations with coordinates, types and magnetic moments of atoms together with the corresponding energies E_k^{DFT} , forces $\mathbf{f}_{i,k}^{\text{DFT}}$ and stresses $\sigma_{ab,k}^{\text{DFT}}$ calculated with DFT for each configuration k . The weights w_e , w_f , and w_s in the loss function are non-negative numbers that control the relative importance of training on energies, forces, and stresses, respectively. To minimize the loss function, the Broyden-Fletcher-Goldfarb-Shanno (BFGS) algorithm [29, 30, 31, 32] with a random initial guess was used.

During simulations using mMTP, prior to each molecular dynamics or geometry optimization step, equilibrium magnetic moments are obtained by minimizing the energy as a function of the atomic magnetic moments. Consequently, for robust simulations, mMTP should accurately describe the potential energy surface for non-equilibrium magnetic moments in the vicinity of the equilibrium ones. Therefore, it is particularly important to include configurations with non-equilibrium magnetic moments in the training set and, consequently, to have the capability to perform constrained spin-polarized DFT calculations.

2.2. Active learning algorithm

To automate the process of constructing a training set, one can use an active learning algorithm, which enables selecting the most relevant configurations during atomic simulations for subsequent recalculation using DFT and

adding the selected configurations to the training set. For non-magnetic MTP the algorithm was formulated in [33, 34], and for mMTP in [18].

Assuming that we have a vector of optimal trainable parameters $\bar{\theta}$ after training only on energies, we can linearize each term in the loss function:

$$E_k^{\text{DFT}} - E_k^{\text{mMTP}}(\boldsymbol{\theta}) \approx E_k^{\text{DFT}} - \sum_{p=1}^P \frac{\partial E_k^{\text{mMTP}}(\bar{\boldsymbol{\theta}})}{\partial \theta_p} (\theta_p - \bar{\theta}_p). \quad (9)$$

After this, one can think of learning the potential as solving a system of equations for $\boldsymbol{\theta}$:

$$\sum_{p=1}^P \theta_p \frac{\partial E_k^{\text{mMTP}}(\bar{\boldsymbol{\theta}})}{\partial \theta_p} = E_k^{\text{DFT}} + \sum_{p=1}^P \bar{\theta}_p \frac{\partial E_k^{\text{mMTP}}(\bar{\boldsymbol{\theta}})}{\partial \theta_p}. \quad (10)$$

Thus, the matrix of the system of equations has the shape $K \times P$, where K denotes the number of configurations $\text{cfg}^{(1)}, \dots, \text{cfg}^{(K)}$ in the training set and P is the number of trainable parameters:

$$B = \begin{pmatrix} \frac{\partial E^{\text{mMTP}}}{\partial \theta_1}(\bar{\boldsymbol{\theta}}, \text{cfg}^{(1)}) & \dots & \frac{\partial E^{\text{mMTP}}}{\partial \theta_P}(\bar{\boldsymbol{\theta}}, \text{cfg}^{(1)}) \\ \vdots & \ddots & \vdots \\ \frac{\partial E^{\text{mMTP}}}{\partial \theta_1}(\bar{\boldsymbol{\theta}}, \text{cfg}^{(K)}) & \dots & \frac{\partial E^{\text{mMTP}}}{\partial \theta_P}(\bar{\boldsymbol{\theta}}, \text{cfg}^{(K)}) \end{pmatrix}. \quad (11)$$

After this, it is possible to select a submatrix A of size $P \times P$ with the maximum absolute value of determinant from the matrix B using the maxvol algorithm [19]. This can be interpreted as searching for the most diverse configurations from the training set.

After constructing the matrix A , an extrapolation grade $\gamma(\text{cfg}^*)$ of each encountered configuration cfg^* can be assessed during atomic simulations:

$$\gamma(\text{cfg}^*) = \max_{1 \leq j \leq P} |c_j|. \quad (12)$$

The vector $\mathbf{c} = (c_1, \dots, c_m)$ is defined as:

$$\mathbf{c} = \left(\frac{\partial E^{\text{mMTP}}}{\partial \theta_1}(\bar{\boldsymbol{\theta}}, \text{cfg}^*), \dots, \frac{\partial E^{\text{mMTP}}}{\partial \theta_P}(\bar{\boldsymbol{\theta}}, \text{cfg}^*) \right) A^{-1}. \quad (13)$$

The extrapolation grade for configuration cfg^* can be interpreted as an indicator of how much the absolute value of the determinant of matrix A grows when configuration cfg^* is added to the training set, i.e. how much the diversity of the training set increases. When $\gamma(\text{cfg}^*) < 1$, it is considered that the potential interpolates the energy value of the configuration cfg^* , and when $\gamma(\text{cfg}^*) > 1$, on the contrary, it extrapolates.

To avoid selecting configurations with an extrapolation grade that is too high or too low, a two-threshold scheme is used, in which configurations with $\gamma(\text{cfg}^*) > \gamma_{\text{low}}$ are preselected and the preselection (or, extrapolation control) stops completely if a configuration with $\gamma(\text{cfg}^*) > \gamma_{\text{up}}$ is encountered. After the simulation is terminated, the matrix A is updated using the maxvol algorithm with configurations from the set of selected configurations. For new configurations included in the matrix A , the energies, forces, and stresses are calculated using DFT, after which these configurations are added to the training set.

For the active learning workflow to work correctly, the configurations calculated using DFT should correspond as closely as possible to the selected ones. Therefore, constraints on the magnetic moments should be satisfied with the highest possible accuracy during DFT calculations. To that end, we use soft-constrained DFT calculations (see subsection 2.3) and add the calculated configurations to the training set. The potential is further trained on the updated training set, after which a new iteration of active learning begins. The active learning algorithm finishes when the simulation does not encounter a single configuration with an extrapolation grade higher than γ_{low} .

2.3. Soft-constrained spin-polarized density functional theory calculations

In conventional (ground state) spin-polarized DFT, we minimize the Hohenberg-Kohn total energy functional $E[\rho; \mathbf{R}, Z, L]$ with respect to the electron density $\rho = \rho(\mathbf{r})$:

$$\rho(\mathbf{r}) = \sum_{i=1}^{N_e} \int \psi_i^{\uparrow*}(\mathbf{r})\psi_i^{\uparrow}(\mathbf{r})d^3\mathbf{r} + \sum_{i=1}^{N_e} \int \psi_i^{\downarrow*}(\mathbf{r})\psi_i^{\downarrow}(\mathbf{r})d^3\mathbf{r} = \rho^{\uparrow}(\mathbf{r}) + \rho^{\downarrow}(\mathbf{r}), \quad (14)$$

where $\psi_i^{\uparrow}(\mathbf{r})$ and $\psi_i^{\downarrow}(\mathbf{r})$ are the electron wavefunctions corresponding to the spin up and spin down electrons, respectively. By solving the following minimization problem:

$$E_{\text{opt}}^{\text{DFT}} \equiv E_{\text{opt}}^{\text{DFT}}(\mathbf{R}, Z, L) = \min_{\rho} E[\rho; \mathbf{R}, Z, L], \quad (15)$$

we obtain the optimal electron density $\rho_{\text{opt}} = \rho_{\text{opt}}^{\uparrow} + \rho_{\text{opt}}^{\downarrow}$ and the optimal energy $E_{\text{opt}}^{\text{DFT}}$. We note that positions of nuclei \mathbf{R} , lattice vectors L , and atomic types Z are fixed when solving equation (15). Using the optimal electron densities $\rho_{\text{opt}}^{\uparrow}$ and $\rho_{\text{opt}}^{\downarrow}$, the magnetic moment of the i -th atom can be calculated by integrating over a specific sphere Ω_i around the i -th atom:

$$\mathbf{m}_i^{\text{opt}} = \int_{\Omega_i} \rho_{\text{opt}}^{\text{mag}}(\mathbf{r})d\mathbf{r} \equiv \int_{\Omega_i} (\rho_{\text{opt}}^{\uparrow}(\mathbf{r}) - \rho_{\text{opt}}^{\downarrow}(\mathbf{r}))d\mathbf{r}. \quad (16)$$

In the case of conventional spin-polarized DFT calculations, the resulting magnetic moments $\mathbf{m}_i^{\text{opt}}, i = 1, \dots, N_{\text{atoms}}$ depend on the ground-state magnetic density $\rho_{\text{opt}}^{\text{mag}}(\mathbf{r})$, i.e. they are equilibrium. Therefore, one cannot generate a training set containing non-equilibrium magnetic moments, which are required for mMTP fitting. Moreover, it is not possible to conserve the magnetic moments close to the selected target values $\mathbf{m}_i^{\text{target}}$ chosen during active learning.

In this study, we used soft-constrained spin-polarized DFT calculations to obtain the resulting non-equilibrium magnetic moments $\mathbf{m}_i = \int_{\Omega_i} \rho^{\text{mag}}(\mathbf{r})d\mathbf{r}$ close to the target magnetic moments $\mathbf{m}_i^{\text{target}}$. The underlying concept of this scheme is the following:

1. Minimize a functional:

$$E^{\text{DFT}} = \min_{\rho} \left(E[\rho; \mathbf{R}, Z, L] + \lambda \sum_{i=1}^{N_{\text{atoms}}} (\mathbf{m}_i - \mathbf{m}_i^{\text{target}})^2 \right), \quad (17)$$

where λ is the chosen penalty weight.

2. Introduce one or several criteria to stop calculations, e.g.

$$\max_i |\mathbf{m}_i - \mathbf{m}_i^{\text{target}}| < \Delta M_{\text{max}}, \quad (18)$$

where ΔM_{max} is the maximum difference between the absolute values of the target and the calculated magnetic moments. If (18) is not valid, then increase λ and minimize the functional (17) starting from the density and, therefore, the magnetic moments obtained in the previous step.

3. Continue step 2 until the criterion for maximum difference (18) in magnetic moments is satisfied, i.e. magnetic moments are close to the target ones.

After the above procedure, we obtain magnetic moments close to the target ones and the DFT energies, forces, and stresses corresponding to these magnetic moments. This procedure enables us to calculate the configurations selected during any atomistic simulation using the active learning (AL) algorithm at the fixed atomic positions, atomic types, lattice vectors, and magnetic moments.

Unlike in the paper [18] where we used hard constraint DFT (cDFT) calculations implemented in the ABINIT code, here we used soft-constrained DFT calculations implemented in VASP. As we demonstrate below on the example of Fe-Pd, even soft-constrained spin-polarized calculations are sufficient for automated construction of a training set for fitting of magnetic MTP.

We note that the primary goal of soft-constrained DFT calculations is to constrain non-equilibrium magnetic moments m_i . However, in VASP it is only possible to constrain the so-called smoothed magnetic moments. As a result, additional computational techniques are required to link the smoothed and target moments. For further details and a complete description of the methodology implemented, see subsection S1.3 in Supplementary Information.

2.4. Workflow for mMTP fitting on soft-constrained DFT calculations

The general scheme of the fitting of mMTP on soft-constrained DFT calculations algorithm is shown in Fig. 1. Before active learning commences, potential is pretrained. Configurations derived from DFT molecular dynamics are utilized as an initial training set. After this, the active learning cycle itself is initiated, wherein the pretrained potential is used in a simulation (here, during molecular dynamics (MD) simulations) with preselection (extrapolation control) of configurations on the basis of extrapolation grade (12). If at least one configuration has been preselected, then the selection of the most diverse configurations from the preselected pool is conducted. After that, DFT calculations for the selected configurations are performed in several stages. At the beginning, DFT calculations are carried out without constraints in order to determine the equilibrium magnetic moments and initial magnetic density for the next stage of DFT calculations. Next, a set of soft-constrained DFT calculations is carried out with a gradual increase in the penalty weight λ and, in the case of convergence, the resulting magnetic moments m_i are close to the target ones m_i^{target} . After completion of the soft-constrained DFT calculations, the converged configurations are added to the training set, the potential is further retrained, after which the updated potential is used in modeling with preselection. The active learning cycle continues until no configuration is preselected. After that, the trained potential can be used to calculate the desired properties of materials.

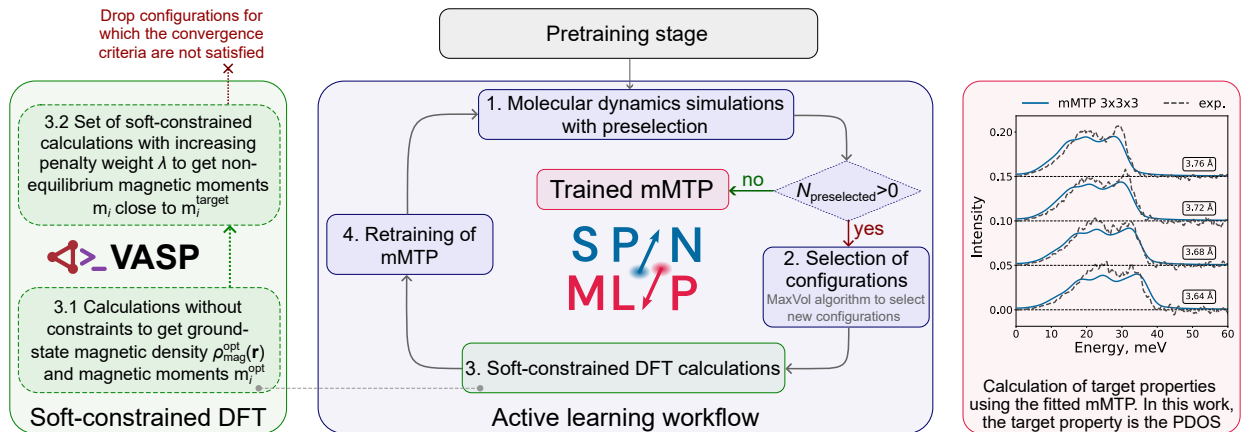


Figure 1: Workflow of mMTP training incorporating soft-constrained DFT calculations. The upper gray panel shows the pretraining stage, in which an initial mMTP is trained on DFT data, such as DFT MD trajectories. The central blue panel illustrates the active-learning loop: (1) MD simulations proceed until no one configuration is preselected; (2) otherwise, selection of configurations from the pool of preselected configurations is conducted; (3) soft-constrained DFT calculations are performed for the selected configurations; (4) further retraining of mMTP is carried out on the updated training set. The left green panel details the soft-constrained workflow: (3.1) DFT calculations without constraints to obtain the ground-state magnetic density $\rho_{\text{opt}}^{\text{mag}}$ and magnetic moments m_i^{opt} ; (3.2) a set of soft-constrained DFT calculations with increasing penalty weight λ to get non-equilibrium magnetic moments m_i close to the target ones m_i^{target} . The right red panel illustrates the subsequent property calculations performed using the fitted mMTP, which in this work corresponds to the projected density of states (PDOS).

3. Results and discussion

3.1. Computational details

An initial training set was created with MD simulations using VASP at 300 K in the NVT ensemble with 22 Fe atoms and 10 Pd atoms in a supercell and at eight different lattice parameters of 3.88, 3.84, 3.80, 3.76, 3.72, 3.68, 3.64, and 3.60 Å. Each MD simulation lasted for several picoseconds (ps) with an MD time step of 1 femtosecond (fs). We

then took each fifth configuration from each trajectory and constructed an initial training set of 5823 configurations with equilibrium magnetic moments.

We fitted mMTP of the 12-th level with $N_\psi = 2$ magnetic and $N_\phi = 8$ radial basis functions as defined in (5). The model has 415 trainable parameters and a cutoff radius R_{cut} of 4 Å.

Active learning was performed during NVT molecular dynamics at 300 K. The ferromagnetic state was used to set the initial magnetic moments for mMTP. Within each active learning iteration, configurations were preselected from several trajectories at different volumes. This leads to a substantial increase in the number of candidates and lengthens the selection process of preselected configurations. To avoid this, here stricter thresholds of $\gamma_{\text{low}} = 3$ and $\gamma_{\text{up}} = 5$ were used instead of the typical thresholds of 2 and 10 utilized in most of the previous papers (see, e.g. [35]). Each MD time step is preceded by a search for equilibrium magnetic moments. Magnetic moment optimization (equilibration) is completed when the norms of all magnetic forces do not exceed 0.001 eV per Bohr magneton. Thus, preselection of configurations occurs both during the equilibration of magnetic moments and during changes in atomic positions during molecular dynamics. This approach ensures that the training set includes enough diversity for both magnetic and spatial degrees of freedom.

To calculate configurations for a training set, we conducted DFT calculations using the projected augmented plane wave method, with the Vienna ab initio Simulation Package (VASP) [25, 26]. All the calculations were performed within the generalized gradient approximation (GGA) in the Perdew–Burke–Ernzerhof (PBE) form [36, 37] for the exchange–correlation (XC) functional. The electron–ion interaction was described with the projector augmented wave (PAW) method [38], using the potentials of version 54. The plane-wave kinetic energy cut-off (E_{cut}) was 500 eV. The k -mesh in the reciprocal space was Gamma-centered with k -spacing less than 0.2 \AA^{-1} for all crystal lattices. The convergence criterion for forces in the non-constrained calculations was 10^{-6} eV. Methfessel-Paxton smearing with the order of 1 with smearing width of 0.1 eV was used for Brillouin-zone integration. Further details of DFT/soft-constrained DFT calculations are described in Supplementary Information in Section S1.

The active learning procedure consisted of 9 iterations, resulting in the addition of 153 configurations to the training set. The distribution of selected configurations across active learning iterations is shown in Fig. 2.

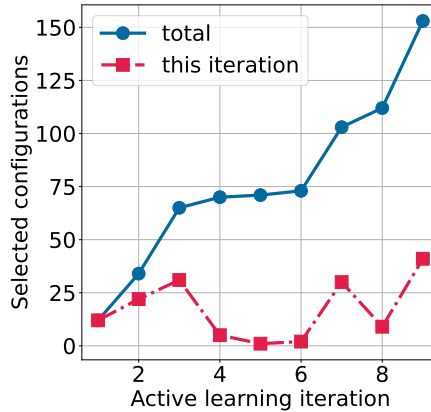


Figure 2: The number of selected configurations during active learning in total and at each iteration

After the active learning stage, NVT molecular dynamics simulations were performed to compute the velocity autocorrelators for the subsequent calculation of the phonon DOS. Each simulation of 50 000 steps was run at 300 K for a specific lattice constant within the range of 3.60 to 3.88 Å with a step of 0.04 Å.

3.2. Fitting errors

A comparison of training errors before and after active learning for the mMTP potential is presented in Table 1. A slight increase in the energy training root mean square error (RMSE) can be observed after active learning, which may be due to the addition of selected configurations with non-equilibrium magnetic moments to the training set.

Table 1: Training root mean square errors (RMSEs) for energies, forces, and stresses before and after active learning.

		before AL	after AL
Training error	E, meV/atom	1.61	1.86
	F, meV/Å	109.5	109.0
	S, GPa	0.44	0.43

3.3. Magnetization

Experimental findings for $\text{Fe}_{0.68}\text{Pd}_{0.32}$ reveal a pressure-induced reduction in magnetization of this crystal with increasing pressure [39, 40]. The dependence of magnetization on the lattice parameter, as well as the pressure on the lattice parameter in comparison with the experiment from [40] is shown in Fig. 3. The values of magnetization and pressure were obtained by averaging over iterations in molecular dynamics after thermalization. Both DFT and trained mMTP qualitatively reproduce the experimentally observed decrease in magnetization with increasing pressure (decreasing lattice parameter). The results for magnetization and pressure dependence obtained using mMTP are in good agreement with DFT-calculated values, except for the magnetization at the two smallest lattice parameters. Since the ferromagnetic state was chosen to define the initial magnetic moments, and equilibrating magnetic moments using mMTP does not result in spin flips, unlike DFT, this leads to an overestimation of the magnetization. For mMTP, MD simulations including Monte Carlo (MC) spin flips (MDMC) could be used to find the global energy minimum; however, such an approach is beyond the scope of this study.

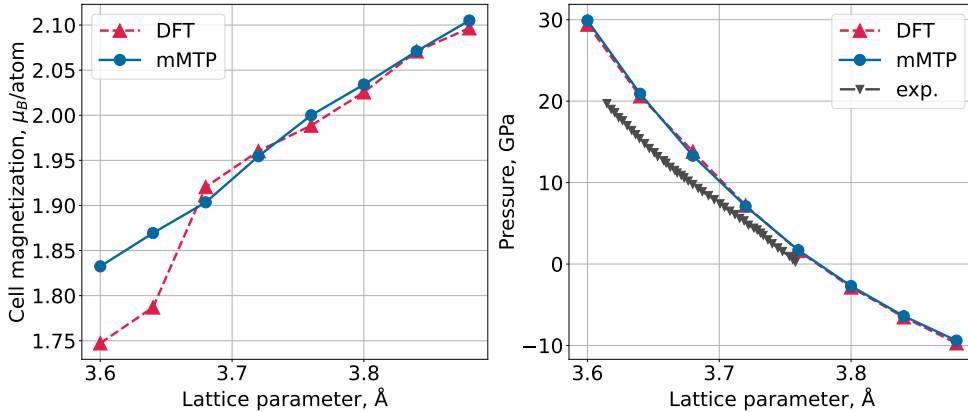


Figure 3: Dependence of magnetization and pressure on lattice parameter at $T = 300$ K. The experimental data were taken from [40].

3.4. Density of states

For eight lattice parameters in the range from 3.60 to 3.88 Å, molecular dynamics was performed in the NVT ensemble at a temperature of 300 K using different numbers of atoms in the Fe-Pd supercell. Phonon density of states (DOS) was computed by taking the Fourier transform of the velocity autocorrelation function. A comparison of the phonon DOS obtained from mMTP and DFT for non-replicated cell (i.e., 32 atoms) is shown in Fig. 4. While the DOS obtained from mMTP agrees well with the DFT benchmark across most frequencies, a slight deviation is observed in the long-wavelength region. This artifact, manifesting as a peak near zero energy, is effectively eliminated by employing larger supercells.

We also present the Fe phonon density of states for $\text{Fe}_{0.68}\text{Pd}_{0.32}$ in Fig. 5, comparing it with the experimental results from work [40]. Simulations with mMTP were carried out with a replicated $3 \times 3 \times 3$ cell comprising 864

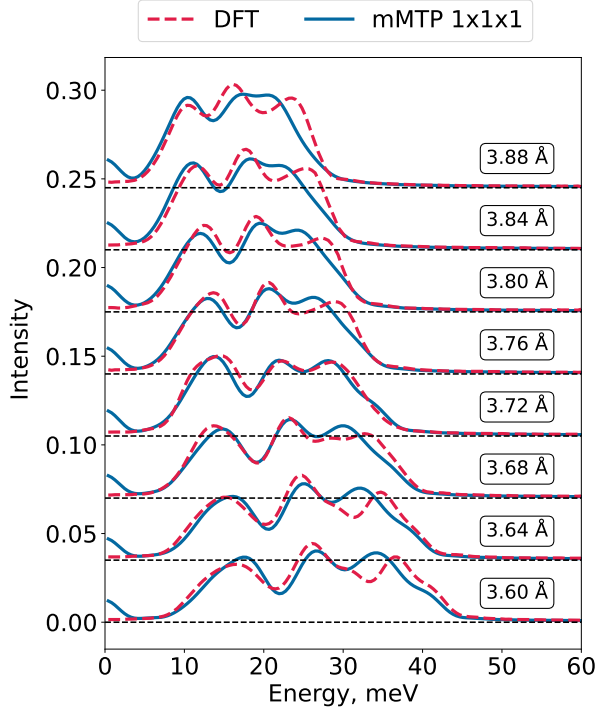


Figure 4: Total phonon DOS for $\text{Fe}_{0.68}\text{Pd}_{0.32}$ calculated with mMTP and DFT for different lattice parameters at 300 K.

atoms and lattice parameters were chosen close to the experimental values. We observe that mMTP correctly captures the qualitative evolution of the DOS with pressure, namely its shift toward higher frequencies as the lattice parameter decreases.

4. Conclusion

In this work, we presented the workflow for active learning of magnetic Moment Tensor Potential (mMTP) during molecular dynamics simulations on the data obtained with density functional theory (DFT) and soft-constrained DFT calculations. Active learning of mMTP was implemented and conducted in the spin-MLIP package [20], molecular dynamics (MD) simulations were carried out in LAMMPS [22, 23], and DFT calculations were performed in the VASP package [25, 26].

The proposed methodology was tested for active training of mMTP on $\text{Fe}_{0.68}\text{Pd}_{0.32}$. A training set of 5976 configurations including 153 configurations with non-equilibrium magnetic moments which were calculated with soft-constrained DFT was prepared. The training errors for energy, forces, and stresses after active learning are 1.86 meV/atom, 109 meV/Å, and 0.43 GPa, respectively. We used this actively trained potential to model the phonon density of states (DOS) and cell magnetization at lattice parameters from 3.60 to 3.88 Å with NVT molecular dynamics at 300 K. The cell magnetization obtained using mMTP is in excellent agreement with the DFT values except for the lattice parameters of 3.60 and 3.64 Å. A possible reason for this discrepancy is that the equilibration of magnetic moments starting from the ferromagnetic state using mMTP does not result in spin flips, unlike DFT. This leads to an overestimation of the magnetization with mMTP for compressed cells. The phonon DOSs calculated with mMTP are consistent with the experimental data. We observed that mMTP correctly captures the shift of DOSs toward higher frequencies as the lattice parameter decreases (or, pressure increases).

In future, the described workflow for active learning together with soft-constrained DFT calculations can be generalized to non-collinear magnetic potentials with configuration selection being performed during spin-lattice dynamics. Another possible direction is an implementation of molecular dynamics (MD) simulations including Monte Carlo

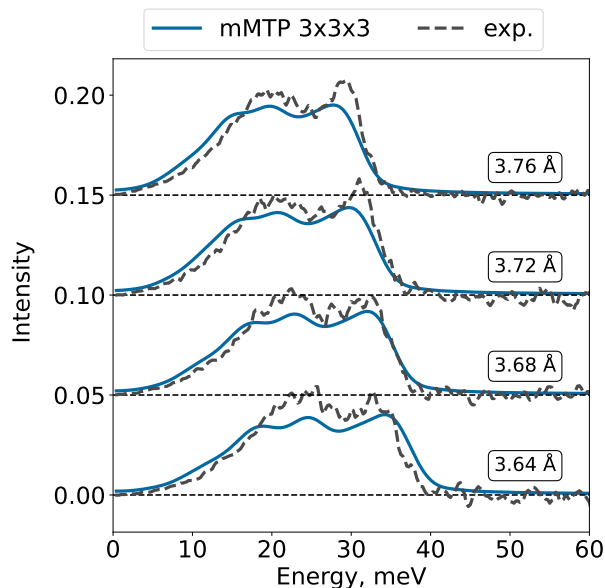


Figure 5: Fe phonon DOS for $\text{Fe}_{0.68}\text{Pd}_{0.32}$ calculated with mMTP and compared with experiment from [40] for different corresponding lattice parameters at 300 K.

(MC) spin flips (MDMC) which enables finding deeper energy minima and achieve results that better agree with the DFT ones.

5. Acknowledgments

The publication was prepared within the framework of the Academic Fund Program at HSE University (grant No. 26-00-054 “Machine learning in atomistic modeling”). This research was supported in part by computational resources of HPC facilities at the HSE University [41].

6. Supplementary information

Details of soft-constrained spin-polarized DFT calculations are given in supplementary information.

7. Conflict of interest

The authors have no conflict of interest to disclose.

8. Data availability

The spin-MLIP package is available at [20] and its interface with the LAMMPS code is available at [21]. We also provide a tutorial available at the link [24] with an example of active learning of mMTPs on DFT/soft-constrained DFT calculations for the Fe-Pd crystal. Finally, the training set as well as the fitted mMTP are available at the same link.

References

- [1] Kangming Li, Chu-Chun Fu, and Anton Schneider. Effects of magnetic excitations and transitions on vacancy formation: cases of fcc fe and ni compared to bcc fe. Physical Review B, 104(10):104406, 2021.
- [2] Marco Eckhoff and Jörg Behler. High-dimensional neural network potentials for magnetic systems using spin-dependent atom-centered symmetry functions. npj Computational Materials, 7(1):170, 2021.
- [3] Jacob BJ Chapman and Pui-Wai Ma. A machine-learned spin-lattice potential for dynamic simulations of defective magnetic iron. Scientific Reports, 12(1):22451, 2022.
- [4] Svetoslav Nikolov, Mitchell A Wood, Attila Cangi, Jean-Bernard Maillet, Mihai-Cosmin Marinica, Aidan P Thompson, Michael P Desjarlais, and Julien Tranchida. Data-driven magneto-elastic predictions with scalable classical spin-lattice dynamics. npj Computational Materials, 7(1):153, 2021.
- [5] Michelangelo Domina, Matteo Cobelli, and Stefano Sanvito. Spectral neighbor representation for vector fields: Machine learning potentials including spin. Physical Review B, 105(21):214439, 2022.
- [6] Hongyu Yu, Yang Zhong, Liangliang Hong, Changsong Xu, Wei Ren, Xingao Gong, and Hongjun Xiang. Spin-dependent graph neural network potential for magnetic materials. Physical Review B, 109(14):144426, 2024.
- [7] Ivan Novikov, Blazej Grabowski, Fritz Körmann, and Alexander Shapeev. Magnetic moment tensor potentials for collinear spin-polarized materials reproduce different magnetic states of bcc fe. npj Computational Materials, 8(1):13, 2022.
- [8] Hongyu Yu, Boyu Liu, Yang Zhong, Liangliang Hong, Junyi Ji, Changsong Xu, Xingao Gong, and Hongjun Xiang. Physics-informed time-reversal equivariant neural network potential for magnetic materials. Physical Review B, 110(10):104427, 2024.
- [9] Matteo Rinaldi, Matous Mrovec, Anton Bochkarev, Yury Lysogorskiy, and Ralf Drautz. Non-collinear magnetic atomic cluster expansion for iron. npj Computational Materials, 10(1):12, 2024.
- [10] Zilong Yuan, Zhiming Xu, He Li, Xinle Cheng, Honggeng Tao, Zechen Tang, Zhiyuan Zhou, Wenhui Duan, and Yong Xu. Equivariant neural network force fields for magnetic materials. Quantum Frontiers, 3(1):8, 2024.
- [11] Teng Yang, Zefeng Cai, Zhengtao Huang, Wenlong Tang, Ruosong Shi, Andy Godfrey, Hanxing Liu, Yuanhua Lin, Ce-Wen Nan, Meng Ye, et al. Deep learning illuminates spin and lattice interaction in magnetic materials. Physical Review B, 110(6):064427, 2024.
- [12] Yunhao Fan, Sheng Zhang, and Gia-Wei Chern. Coarsening of chiral domains in itinerant electron magnets: A machine learning force-field approach. Physical Review B, 110(24):245105, 2024.
- [13] Matteo Rinaldi, Matous Mrovec, Anton Bochkarev, Yury Lysogorskiy, and Ralf Drautz. Non-collinear magnetic atomic cluster expansion for iron. npj Computational Materials, 10(1):12, 2024.
- [14] Yuqiang Gao, Menno Bokdam, and Paul J Kelly. Machine learning exchange fields for ab-initio spin dynamics. arXiv preprint arXiv:2403.10769, 2024.
- [15] <https://github.com/yangtengleo/DeepSPIN/>.
- [16] <https://github.com/mttrin93/mag-ace/>.
- [17] Alexey S Kotykhov, Konstantin Gubaev, Max Hodapp, Christian Tantardini, Alexander V Shapeev, and Ivan S Novikov. Constrained dft-based magnetic machine-learning potentials for magnetic alloys: a case study of fe–al. Scientific Reports, 13(1):19728, 2023.
- [18] Alexey S Kotykhov, Max Hodapp, Christian Tantardini, Konstantin Kravtsov, Ivan Kruglov, Alexander V Shapeev, and Ivan S Novikov. Actively trained magnetic moment tensor potentials for mechanical, dynamical, and thermal properties of paramagnetic crn. Physical Review B, 111(9):094438, 2025.

- [19] Sergei A Goreinov, Ivan V Oseledets, Dimitry V Savostyanov, Eugene E Tyrtshnikov, and Nikolay L Zamarashkin. How to find a good submatrix. In Matrix Methods: Theory, Algorithms And Applications: Dedicated to the Memory of Gene Golub, pages 247–256. World Scientific, 2010.
- [20] <https://gitlab.com/ivannovikov/spin-mlip/>.
- [21] <https://gitlab.com/ivannovikov/interface-lammps-spin-mlip/>.
- [22] Steve Plimpton. Fast parallel algorithms for short-range molecular dynamics. Journal of computational physics, 117(1):1–19, 1995.
- [23] Aidan P Thompson, H Metin Aktulga, Richard Berger, Dan S Bolintineanu, W Michael Brown, Paul S Crozier, Pieter J In't Veld, Axel Kohlmeyer, Stan G Moore, Trung Dac Nguyen, et al. Lammps-a flexible simulation tool for particle-based materials modeling at the atomic, meso, and continuum scales. Computer Physics Communications, 271:108171, 2022.
- [24] <https://gitlab.com/accat/spin-mlip-active-learning-with-soft-constrained-dft-tutorial/>.
- [25] G. Kresse and J. Furthmüller. Efficient iterative schemes for ab initio total-energy calculations using a plane-wave basis set. Phys. Rev. B, 54:11169–11186, 1996.
- [26] G. Kresse and D. Joubert. From ultrasoft pseudopotentials to the projector augmented-wave method. Phys. Rev. B, 59:1758–1775, 1999.
- [27] Alexander V Shapeev. Moment tensor potentials: A class of systematically improvable interatomic potentials. Multiscale Modeling & Simulation, 14(3):1153–1173, 2016.
- [28] Konstantin Gubaev, Evgeny V Podryabinkin, Gus LW Hart, and Alexander V Shapeev. Accelerating high-throughput searches for new alloys with active learning of interatomic potentials. Computational Materials Science, 156:148–156, 2019.
- [29] Charles George Broyden. The convergence of a class of double-rank minimization algorithms 1. general considerations. IMA Journal of Applied Mathematics, 6(1):76–90, 1970.
- [30] Roger Fletcher. A new approach to variable metric algorithms. The computer journal, 13(3):317–322, 1970.
- [31] Donald Goldfarb. A family of variable-metric methods derived by variational means. Mathematics of computation, 24(109):23–26, 1970.
- [32] David F Shanno. Conditioning of quasi-newton methods for function minimization. Mathematics of computation, 24(111):647–656, 1970.
- [33] Evgeny V Podryabinkin and Alexander V Shapeev. Active learning of linearly parametrized interatomic potentials. Computational Materials Science, 140:171–180, 2017.
- [34] Konstantin Gubaev, Evgeny V Podryabinkin, and Alexander V Shapeev. Machine learning of molecular properties: Locality and active learning. The Journal of chemical physics, 148(24):241727, 2018.
- [35] Ivan S Novikov, Yury V Suleimanov, and Alexander V Shapeev. Automated calculation of thermal rate coefficients using ring polymer molecular dynamics and machine-learning interatomic potentials with active learning. Physical Chemistry Chemical Physics, 20(46):29503–29512, 2018.
- [36] John P. Perdew, Kieron Burke, and Matthias Ernzerhof. Generalized gradient approximation made simple. Phys. Rev. Lett., 77:3865–3868, 1996.
- [37] John P. Perdew, Kieron Burke, and Matthias Ernzerhof. Generalized gradient approximation made simple. Phys. Rev. Lett., 78:1396–1396, 1997.

- [38] P. E. Blöchl. Projector augmented-wave method. Phys. Rev. B, 50:17953–17979, 1994.
- [39] M Matsushita, T Nishimura, S Endo, M Ishizuka, Koichi Kindo, and F Ono. Anomalous magnetic moments in fe-pt and fe-pd invar alloys under highpressure. Journal of Physics: Condensed Matter, 14(44):10753, 2002.
- [40] ER Priesen Reis, P Guzman, SH Lohaus, A Lin, CM Bernal-Choban, B Fultz, JY Zhao, G Shen, MY Hu, EE Alp, et al. Thermodynamic origin of the pressure-induced invar effect: General criterion and experimental study of fe 68 pd 32. Physical Review B, 112(14):144416, 2025.
- [41] PS Kostenetskiy, RA Chulkevich, and VI Kozyrev. HPC resources of the higher school of economics. In Journal of Physics: Conference Series, volume 1740, page 012050. IOP Publishing, 2021.

Supplementary Information: Active learning of collinear magnetic Moment Tensor Potentials using the spin-MLIP package from soft-constrained spin-polarized DFT calculations: a case study of Fe-Pd

Our current workflow has been implemented and tested only for conserving collinear magnetic moments, in which all magnetic moments m_i are aligned along a single direction and thus have only one non-zero component, either x , or y , or z . Therefore, we use only scalar magnetic moments m_i instead of the vector \mathbf{m}_i . The requirement to carry out non-collinear calculations arises from limitations in VASP’s implementation of soft-constrained spin-polarized calculations. However, with only minor modifications, our workflow for collinear soft-constrained calculations can be extended to the non-collinear case.

S1. Soft-constrained spin-polarized DFT calculations

S1.1. VASP notations and types of magnetic moments

Table S1: Notation for VASP files, INCAR tags, definitions of different magnetic moment, and other technical terms used in this work.

Notation	Description
VASP files	
INCAR	File with input parameters for the VASP calculations
POTCAR	Pseudopotential with data for all atomic species
OUTCAR	Output file with detailed information about the VASP run
OSZICAR	Convergence information, including M_{int} (m_i^{WS}) and MW_{int} (m_i^{sWS}) at each ionic step
WAVECAR	Wave function file
CHGCAR	Charge density file
INCAR tags	
MAGMOM	Initial magnetic moments assigned to each atom
M_CONSTR	Desired local magnetic moments. The smoothed magnetic moments MW_{int} (m_i^{sWS}) are close to them after the soft-constrained calculations
LNONCOLLINEAR	Enables non-collinear magnetic calculations
I_CONSTRAINED_M	Switches on the constrained local moments approach
LWAVE	Specifies whether the wave function is written
LCHARG	Specifies whether the charge density is written
RWIGS	Wigner-Seitz radius for each atomic type. Used for M_{int} integration
Other notations	
M_{int}	Moment integrated over atom-centered spheres with Wigner-Seitz radius (m_i^{WS})
MW_{int}	Smoothed moments integrated over atom-centered spheres of Wigner-Seitz radius (m_i^{sWS})
Types of magnetic moments	
m_i	Magnetic moments from (PAW) region integration (M , located in OUTCAR)
m_i^{WS}	Magnetic moments from Wigner-Seitz sphere integration (M_{int} , located in OSZICAR)
m_i^{sWS}	Smoothed magnetic moments from Wigner-Seitz sphere integration (MW_{int} , located in OSZICAR)
m_i^{target}	Target magnetic moments (required to retrain mMTP after selection)
m_i^{constr}	Imposed constraint magnitude on smoothed magnetic moments (M_CONSTR , specified in INCAR)
$\tilde{m}_i^{\text{refined}}$	Refined constraint magnitude on smoothed magnetic moments used to achieve $m_i \approx m_i^{\text{target}}$ after the last stage of soft-constrained DFT calculations (M_CONSTR , specified in INCAR)

S1.2. Definitions of VASP magnetic moments

To formulate an algorithm, we introduce the so-called smoothed magnetic moments, which are the only option to constrain in VASP, using the M_CONSTR tag:

$$\mathbf{m}_i^{\text{SWS}} = \int_{\Omega_i^{\text{WS}}} \rho_{\text{mag}}(\mathbf{r}) F_i(|\mathbf{r}|) d\mathbf{r}, \quad (\text{S1})$$

where Ω_i^{WS} is the atom-centered sphere of the radius given by the RWIGS tag, and $F_i(|\mathbf{r}|)$ is a function that equals unity near the center of the sphere and smoothly decays to zero at the boundary.

The corresponding unsmoothed magnetic moments (denoted as M_{int} in OSZICAR) are computed as

$$\mathbf{m}_i^{\text{WS}} = \int_{\Omega_i^{\text{WS}}} \rho_{\text{mag}}(\mathbf{r}) d\mathbf{r}. \quad (\text{S2})$$

The difference between \mathbf{m}_i^{WS} (M_{int}) and $\mathbf{m}_i^{\text{SWS}}$ (MW_{int}) is illustrated in Fig. S1, using arbitrary units for clarity. Both \mathbf{m}_i^{WS} and $\mathbf{m}_i^{\text{SWS}}$ are written in the OSZICAR file.

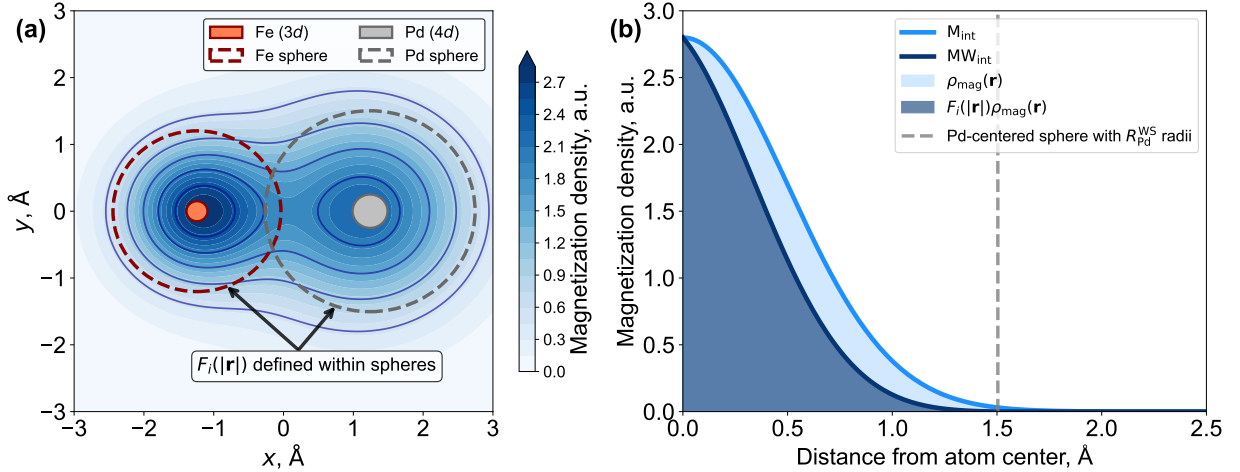


Figure S1: Magnetic density around Fe–Pd atoms and the effect of the smoothing function. (a) Two-dimensional magnetic density $\rho_{\text{mag}}(\mathbf{r})$ (blue) around an Fe atom (red) and a Pd atom (silver), with the projections of the atom-centered spheres onto the xy plane outlined by dashed circles corresponding to the Wigner-Seitz radii, as specified by the RWIGS tag in VASP. (b) Illustration of the origin of the difference between M_{int} and MW_{int} for a Pd atom. Radial magnetic profiles: the raw $\rho_{\text{mag}}(\mathbf{r})$ (sky blue) versus the smoothed product $F_i(|\mathbf{r}|)\rho_{\text{mag}}(\mathbf{r})$ (dark blue). The function $F_i(|\mathbf{r}|)$ ramps from unity at the atomic core to zero at the boundary of the atom-centered sphere. The gray dashed line indicates the Wigner-Seitz radius of the Pd atom ($R_{\text{Pd}}^{\text{WS}}$), up to which the integration of the magnetic density is performed.

There is also a third type of magnetic moments written in OUTCAR file. These moments are integrated over the projected-augmented wave (PAW) regions and obtained by decomposing the Kohn-Sham orbitals into angular-momentum (l) and magnetic quantum number (m) components within the PAW spheres [38]. In this case, (S2) is rewritten as

$$\mathbf{m}_i = \int_{\Omega_i^{\text{PAW}}} \rho_{\text{mag}}(\mathbf{r}) d\mathbf{r}, \quad (\text{S3})$$

where Ω_i^{PAW} denotes the PAW augmentation region around atom i and $\rho_{\text{mag}}(\mathbf{r})$ is the magnetic density. The aim of our algorithm of soft-constrained DFT calculations is to obtain $\mathbf{m}_i \approx \mathbf{m}_i^{\text{target}}$.

S1.3. Scheme and technical aspects of soft-constrained workflow

From a conceptual point of view, the scheme of soft-constrained DFT calculations is defined in 2.3 for m_i and m_i^{target} . However, as it was mentioned in the main text, in practice it is used for m_i^{sWS} due to the specifics of the VASP package. The complete scheme of soft-constrained DFT calculations to get $m_i \simeq m_i^{\text{target}}$ is presented in Fig. S2 and described in the text below.

1. At the beginning, equilibrium self-consistent field calculations (collinear, without constraints on magnetic moments) are performed to obtain an initial approximation of the wave function and ground-state charge density $\rho_{\text{opt}}^{\text{mag}}(\mathbf{r})$, thereby accelerating the subsequent non-collinear calculations.
2. After this, non-collinear soft-constrained self-consistent field calculations are performed to rescale the Wigner-Seitz radii. This step is added because the moments m_i^{sWS} and m_i^{WS} reported in the OSZICAR files are obtained by integrating over atom-centered spheres with Wigner-Seitz radii (the RWIGS tag). The differences in the integration schemes between m_i^{sWS} and m_i lead to a small discrepancy between them. However, this difference can be reduced if the integration spheres cover almost 100 % of the simulation cell by rescaling the Wigner-Seitz radii (more details can be found in subsection S1.4).
3. The next step is a linear fit between the unsmoothed magnetic moments m_i^{WS} and the smoothed magnetic moments m_i^{sWS} , the result of which is used to adapt the initial target magnetic moments m_i^{target} . Due to the smoothing function $F_i(|\mathbf{r}|)$, the constrained magnetic moments m_i^{sWS} always differ from m_i^{target} , which are required to retrain mMTP. Therefore, a scaling of the constrained magnetic moments is necessary. In this work, we use a linear regression between m_i^{sWS} and m_i^{WS} to determine the initial constraining smoothed magnetic moments m_i^{constr} . We do not fit m_i^{sWS} against m_i because, in general, the corresponding R^2 value is lower and the linear relation still depends weakly on λ . For more details on the linear fitting stage, see subsection S1.5.
4. Once we found m_i^{constr} , non-collinear soft-constrained calculations are performed during which the functional is minimized:

$$E^{\text{DFT}} = \min_{\rho} \left(E[\rho; \mathbf{R}, Z, L] + \lambda \sum_{i=1}^{N_{\text{atoms}}} (m_i^{\text{sWS}} - m_i^{\text{constr}})^2 \right). \quad (\text{S4})$$

After minimization, the convergence criteria for magnetic moments are checked (see subsection S1.6). If at least one of the criteria is violated, the λ value increases and the functional (S4) is minimized again, starting from the density and, therefore, the magnetic moments obtained in the previous step. If all the convergence criteria are satisfied at some λ then this configuration is considered as converged and its magnetic moments can be refined. If, after iterating over all available λ , not all criteria are met, the calculation using the lambda with the smallest mean absolute error (MAE) between m_i^{sWS} and m_i^{constr} is selected. A refinement is then always performed, after which the error may become acceptable even without convergence at the λ iteration stage.

5. Finally, magnetic moments are refined. After the soft-constrained calculations, we obtain $m_i^{\text{sWS}} \simeq m_i^{\text{constr}}$. However, the magnetic moments m_i reported in the OUTCAR file slightly differ from the integrated magnetic moment m_i^{WS} in the OSZICAR file due to different integration schemes. The values m_i are obtained by integration over PAW regions, while the m_i^{WS} magnetic moments are computed by radial integration over atom-centered spheres with Wigner-Seitz radii. To eliminate this discrepancy, we adjust the refined constraint moments to $\widetilde{m}_i^{\text{refined}}$ so that, after the final calculation, $m_i \simeq m_i^{\text{target}}$. For more details, see subsection S1.7.

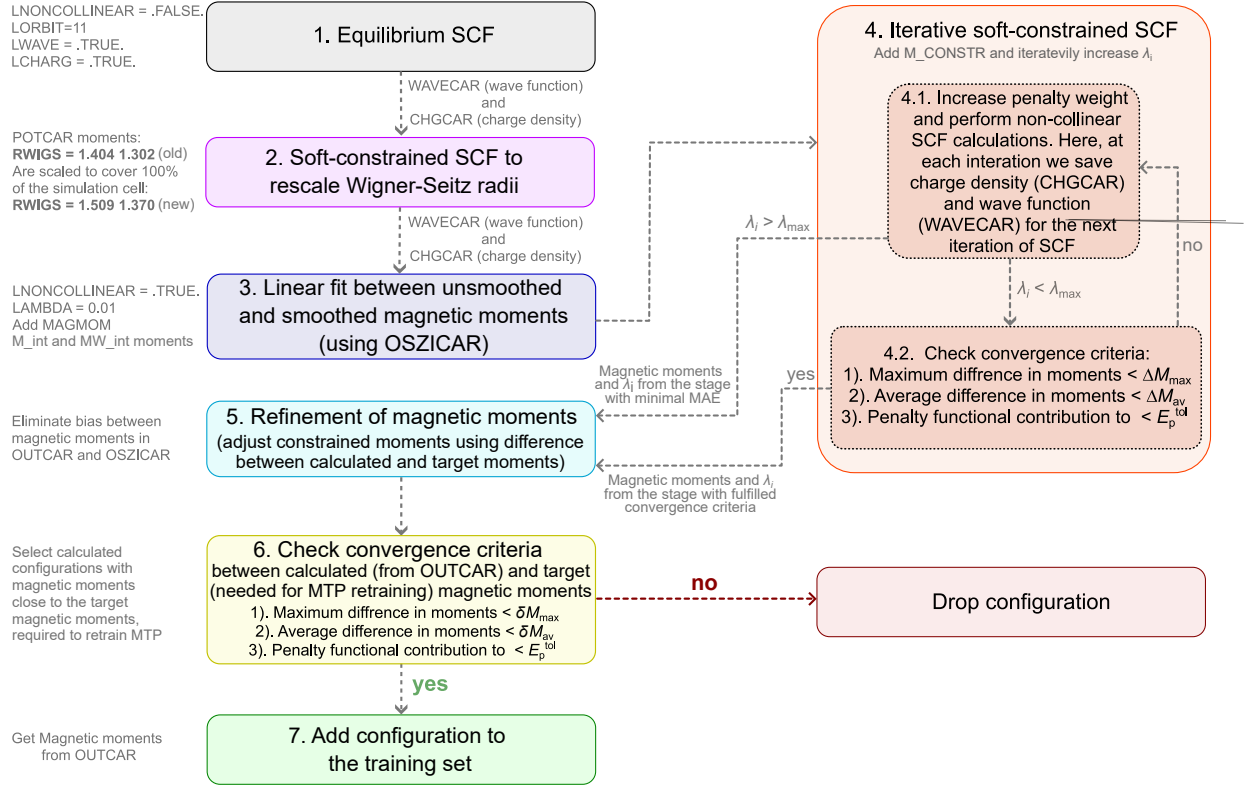


Figure S2: Scheme of soft-constrained DFT calculations. (1) Equilibrium self-consistent field (SCF) calculation. (2) Soft-constrained SCF calculation in which the Wigner-Seitz radii of the atom-centered spheres are rescaled proportionally from their initial values in POTCAR to cover approximately 100 % of the simulation cell. (3) Linear fit is performed between the unsmoothed magnetic moments m_i^{WS} (M_{int}) and the smoothed magnetic moments m_i^{sWS} (MW_{int}). (4) Iterative soft-constrained SCF calculations: the penalty weight λ is increased until the maximum and average magnetic moment differences decrease below ΔM_{\max} and ΔM_{av} , respectively, and the contribution of the penalty functional to the total energy is smaller than E_p^{tol} (see the criteria (S8), (S9), and (S10)). If these criteria are satisfied, the configuration proceeds to the final refinement stage with the current λ_i . Otherwise, if the criteria are not satisfied at $\lambda_i = \lambda_{\max}$, the configuration calculated with the value of λ_i that yields smoothed magnetic moments m_i^{sWS} closest to the constraining smoothed magnetic moments m_i^{constr} is sent for refinement. (5) At the refinement stage, the constrained magnetic moments in INCAR (via the M_CONSTR tag) are adjusted using the difference between the magnetic moments in OSZICAR (M_{int}) and OUTCAR (m_i). After this refinement step, the magnetic moments m_i reported in OUTCAR file are approximately equal to the target moments m_i^{target} . (6) Check the criteria ((S8), (S9), and (S10)) for m_i and m_i^{target} . Configurations that satisfy these criteria are added to the training set (panel 7); otherwise, they are discarded.

S1.4. RWIGS set up

Since the RWIGS tag is essential for computing m_i^{WS} (M_{int}) and m_i^{sWS} (MW_{int}), we cannot avoid using it, even though magnetic moments m_i in OUTCAR can be calculated without this parameter (the tag LORBIT > 11). In this work, we take the initial RWIGS values from the POTCAR files and perform non-collinear calculations to determine the percentage of the simulation cell covered by the atom-centered spheres. Subsequently, we proportionally rescale the Wigner-Seitz radii so that the spheres cover almost 100 % of the cell volume:

$$R_{z_i}^{\text{WS}}(\text{new}) = R_{z_i}^{\text{WS}}(\text{old}) \frac{1}{C^{1/3}}, \quad (\text{S5})$$

where $R_{z_i}^{\text{WS}}(\text{new})$ is the adjusted Wigner-Seitz radius for species z_i , $R_{z_i}^{\text{WS}}(\text{old})$ is the initial Wigner-Seitz radius taken from the POTCAR file, and C is the fraction of the simulation cell volume originally covered by the atom-centered spheres.

If we choose RWIGS radii for all species such that almost 100 % of the simulated cell is covered by atom-centered spheres, the magnetic moments reported in OUTCAR (m_i) and the unsmoothed moments M_{int} become nearly identical. We carry out further calculations with these RWIGS.

S1.5. Linear fitting

In VASP, it is possible to constrain only the smoothed magnetic moments m_i^{sWS} , but $m_i^{\text{sWS}} \neq m_i^{\text{target}}$ because m_i^{sWS} are computed with the smoothing function $F_i(|\mathbf{r}|)$ during integration. We therefore aim to obtain reasonable constraining magnetic moments m_i^{constr} .

To address the problem, we perform a linear fitting between m_i^{WS} and m_i^{sWS} as follows:

$$m_i^{\text{WS}} = k_{\text{fit}}(\lambda)m_i^{\text{sWS}} + b_{\text{fit}}(\lambda), \quad (\text{S6})$$

where k_{fit} and b_{fit} are coefficients of linear fitting.

The results of the linear fitting are shown in Fig. S3.

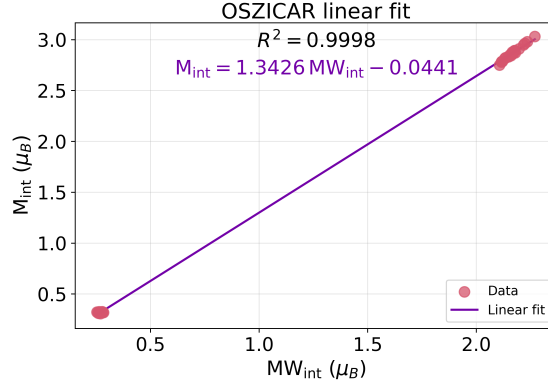


Figure S3: Atom-centered integrated magnetic density at each atomic site m_i^{WS} (M_{int}) as a function of smoothed integrated magnetic density m_i^{sWS} (MW_{int}) which has been smoothed towards the boundary of the sphere. The data was linearly fitted to find coefficients for further interpolation.

In general, the fit parameters k_{fit} and b_{fit} depend on the penalty weight λ . However, as shown in Fig. S4, this dependence is weak. After iterating over a sequence of penalty weights λ , we obtain $m_i^{\text{sWS}} \approx m_i^{\text{constr}}$, and the final refinement step removes the remaining small discrepancy. Henceforth, we use only the values $k_{\text{fit}} = k_{\text{fit}}(\lambda_0)$ and $b_{\text{fit}} = b_{\text{fit}}(\lambda_0)$ obtained at the first lambda weight λ_0 .

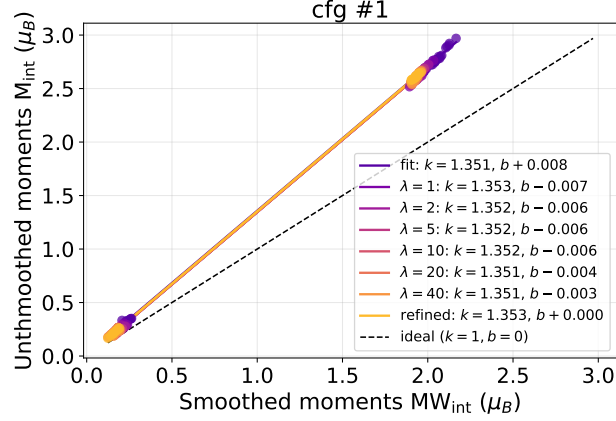


Figure S4: Unsmoothed magnetic moments integrated over atom-centered spheres with Wigner-Seitz radii, m_i^{WS} (M_{int}), as a function of the smoothed magnetic moments m_i^{WS} (MW_{int}). The interpolation coefficients remain nearly constant as the penalty weight λ is increased.

Finally, we can get an initial approximation of constraining moments m_i^{constr} :

$$m_i^{\text{constr}} = (m_i^{\text{target}} - b_{\text{fit}})/k_{\text{fit}}. \quad (\text{S7})$$

S1.6. Convergence criteria

During iterative soft-constrained self-consistent field calculations, the gradual increase of the λ value (see S4) is stopped and configurations are considered as converged when all the following criteria are met:

$$\max_i |m_i^{\text{sWS}} - m_i^{\text{constr}}| < \Delta M_{\text{max}}, \quad (\text{S8})$$

where ΔM_{max} is the threshold for the maximum absolute error (MaxAE),

$$\frac{1}{N_{\text{atoms}}} \sum_{i=1}^{N_{\text{atoms}}} |m_i^{\text{sWS}} - m_i^{\text{constr}}| < \Delta M_{\text{av}}, \quad (\text{S9})$$

where ΔM_{av} is the threshold for MAE,

$$\lambda \sum_{i=1}^{N_{\text{atoms}}} (m_i^{\text{sWS}} - m_i^{\text{constr}})^2 / N_{\text{atoms}} < E_p^{\text{tol}}, \quad (\text{S10})$$

where E_p^{tol} is the maximum permissible contribution to the total energy of the penalty functional. The values of ΔM_{max} , ΔM_{av} , and E_p^{tol} for Fe-Pd investigated here are given in subsection S1.8. Details of the iterative soft-constrained self-consistent field calculations for several configurations of Fe-Pd are shown in subsection S1.9.1. Configurations satisfying all criteria proceed to the refinement stage. Otherwise, we check smoothed magnetic moments m_i^{sWS} obtained for different λ , choose the ones yielding the smallest MAE (S9), and send them to the refinement stage.

S1.7. Final refinement of magnetic moments

To resolve the constant bias between the magnetic moments in OSZICAR (m_i^{WS}) and OUTCAR (m_i) arising from different integration schemes and integration volumes, we refine the M_CONSTR (m_i^{constr}) values in INCAR file. This consists of adjusting the constrained moments M_CONSTR (m_i^{constr}) and rerunning the final calculation using the

penalty weight λ obtained at the end of the iterative soft-constrained stage with the refined magnetic moments $\tilde{m}_i^{\text{refined}}$ (see Fig. S2).

The correction proceeds as follows:

$$\tilde{m}_i^{\text{refined}} = m_i^{\text{constr}} - [m_i - m_i^{\text{WS}}] / k_{\text{fit}}, \quad (\text{S11})$$

where k_{fit} is linear slope from the fitting of m_i^{WS} and m_i^{sWS} .

In VASP notations the correction is:

$$\text{M_CONSTR}(\text{new}) = \text{M_CONSTR}(\text{old}) - [\text{M}(\text{OUTCAR}) - \text{M}_{\text{int}}(\text{OSZICAR})] / k_{\text{fit}}, \quad (\text{S12})$$

where $\text{M_CONSTR}(\text{old})$ and $\text{M_CONSTR}(\text{new})$, are the constrained magnetic moments in INCAR file before and after the refinement procedure, $\text{M}(\text{OUTCAR})$ are magnetic moments in OUTCAR file, $\text{M}(\text{OSZICAR})$ are magnetic moments in the OSZICAR file (M_{int}), and k_{fit} is the coefficient of linear interpolation between M_{int} and MW_{int} (see subsection S1.5). After substituting (S6) and (S7) to (S11) it can be seen that after soft-constrained DFT calculation with $\tilde{m}_i^{\text{refined}}$ we obtain $m_i \simeq m_i^{\text{target}}$ which was our aim. If, after refinement, the criteria in (S8), (S9), and (S10) are satisfied for m_i and m_i^{target} , then the configuration is added to the training set; otherwise, it is discarded. The results of the refinement for several Fe-Pd configurations are demonstrated in subsection S1.9.2.

S1.8. Parameters of soft-constrained DFT calculations for Fe-Pd

The typical penalty weights and criteria thresholds, which we used for Fe-Pd including 32 atoms, are provided in Table S2. The threshold for the penalty functional contribution to the total energy (E_p^{tol}), introduced in (S10), was set below the typical ML potential training error of 1 meV/atom.

Table S2: Parameters used in the Fe-Pd soft-constrained calculations and their values: maximum difference between constrained and computed magnetic moments (ΔM_{max}), mean absolute difference between computed and constraining magnetic moments (ΔM_{av}), maximum allowed penalty energy contribution to the total energy (E_p^{tol}), value of the penalty weight at the zero-shot iteration (λ_0), which is also used for Wigner-Seitz radii adjustment (see subsection S1.4) and for the fitting stage of m_i^{WS} and m_i^{sWS} (see subsection S1.5), and the sequence of penalty weights employed to converge toward the desired magnetic moments (λ).

Parameter	Description	Value
ΔM_{max}	Maximum magnetic moment tolerance (MaxAE)	$3 \times 10^{-2} \mu_{\text{B}}$
ΔM_{av}	Average magnetic moment tolerance (MAE)	$2 \times 10^{-2} \mu_{\text{B}}$
E_p^{tol}	Contribution to the total energy arising from the penalty functional	$1 \times 10^{-2} \text{ eV}$
λ_0	Penalty weight at the zero-shot non-collinear iterations	0.01
λ	Penalty weights used to iteratively converge to the desired moments	[2, 5, 10, 20, 30, 40]

S1.9. Results of soft-constrained DFT calculations

As we have already used the maximum absolute error (MaxAE) and the mean absolute error (MAE) as convergence criteria, we decided not to employ the root mean square error (RMSE) as a stopping criterion in our workflow, because it can be overly excessive for practical use. However, RMSE remains useful during post-processing analysis of the results, and therefore we introduce it as follows:

$$\Delta M_{\text{RMSE}} = \sqrt{\sum_{i=1}^{N_{\text{atoms}}} (m_i^{\text{sWS}} - m_i^{\text{constr}})^2 / N_{\text{atoms}}}.$$

S1.9.1. Iterative soft-constrained self-consistent field calculations stage

Here we provide the results of the iterative soft-constrained self-consistent field calculations stage. From Figures S1.9.1 and S1.9.1 we conclude that the convergence criteria (S8), (S9), and (S10) are valid for two given configurations.

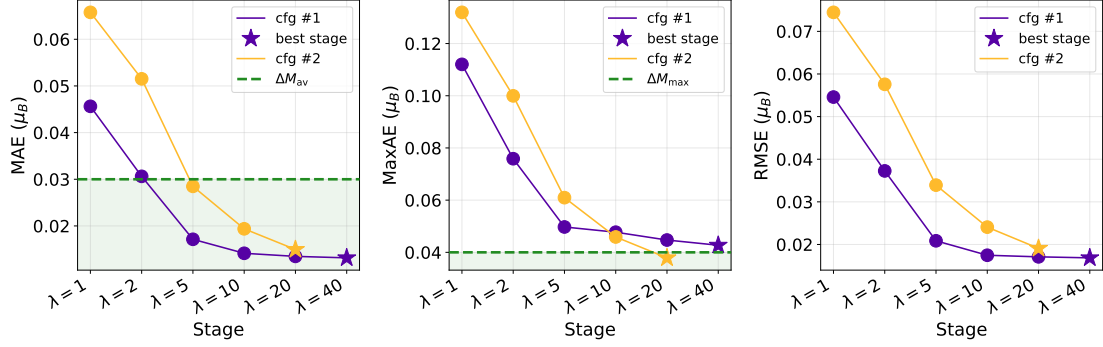


Figure S5: Evolution of the error metrics (MAE, MaxAE, and RMSE) at stages with different penalty weights λ (subsection S1.6). The errors are defined as the difference between the constraining magnetic moments m_i^{constr} (M_CONSTR in OSZICAR) and the calculated smoothed magnetic moments m_i^{sWS} (MW_{int} in OSZICAR). The star symbol indicates the best MAE across all calculations. The green shaded area satisfies the prescribed threshold criteria for MAE (ΔM_{av}) and MaxE (ΔM_{max}). For the first configuration, no calculation with $\lambda = 40$ is shown, because all convergence criteria for MAE and MaxAE were already met at the previous stage with $\lambda = 20$.

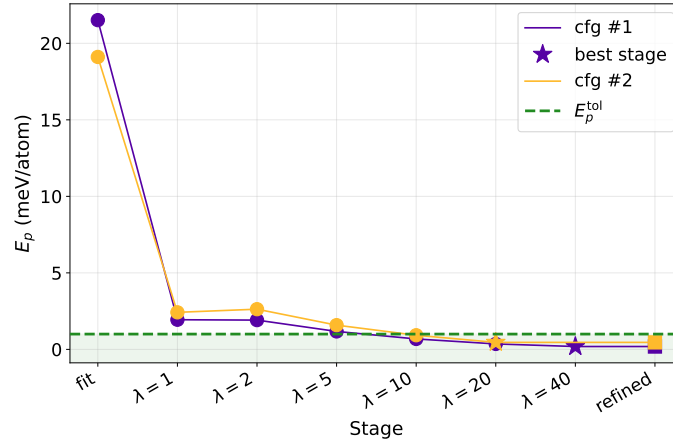


Figure S6: Evolution of the penalty energy E_p across various stages for two randomly chosen configurations: fitting of magnetic moments (subsection S1.5), convergence with different penalty weights λ (subsection S1.6), and the refinement stage (subsection S1.7). The star symbol marks the stage with the best MAE across all considered configurations. The green shaded area indicates where the penalty energy satisfies the threshold criterion E_p^{tol} .

S1.9.2. Refinement stage

Here, we replace the soft-constraint criteria for magnetic moments (M_{av} and M_{max}), which were originally defined between the constraining moments m_i^{constr} and the smoothed moments m_i^{sWS} , with new criteria based on the difference between the calculated magnetic moments m_i and the target magnetic moments m_i^{target} . These new thresholds are denoted as $\delta m_{\text{tol}}^{\text{av}}$ for MAE and $\delta m_{\text{tol}}^{\text{max}}$ for MaxAE.

After refinement, the difference between the calculated magnetic moments m_i and the target moments m_i^{target}

decreases both on average (Fig. S7) and for each individual atom (Fig. S8).

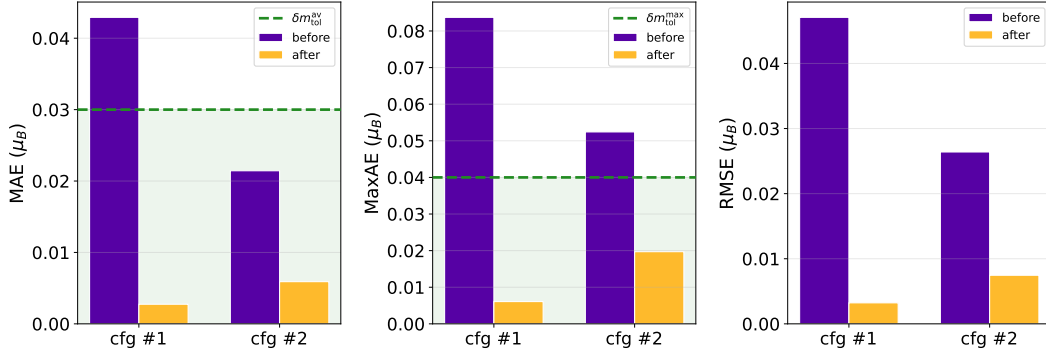


Figure S7: Error metrics (MAE, MaxAE, and RMSE) before and after refinement. Here, the errors are defined as the difference between the target magnetic moments m_i^{target} and the calculated magnetic moments m_i (from OUTCAR). The green shaded area indicates where both MaxAE and MAE satisfy the respective threshold criteria $\delta m_{\text{tol}}^{\text{max}}$ and $\delta m_{\text{tol}}^{\text{av}}$.

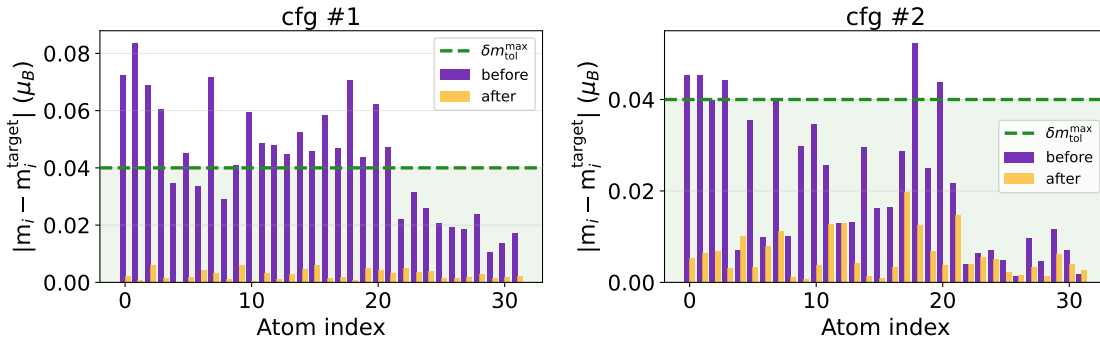


Figure S8: Per-atom results of the magnetic-moment refinement for two configurations. Here, we compare the target magnetic moments m_i^{target} with the calculated magnetic moments m_i (from OUTCAR), which are in the mMTP training. (left) first configuration; (right) second configuration. The green shaded area indicates where MaxAE satisfies the respective threshold $\delta m_{\text{tol}}^{\text{max}}$.

S1.10. Convergence of magnetic moments

Summarizing our workflow, the soft-constrained calculations allow us to obtain the smoothed magnetic moments m_i^{sWS} , as illustrated in Fig. S9. However, due to the different integration schemes used for m_i and m_i^{sWS} , where the latter is linearly fitted to m_i^{sWS} , a small discrepancy remains between the target magnetic moments m_i^{target} (reported in OUTCAR) and the final moments m_i , as shown in Fig. S10. This discrepancy is successfully eliminated after the refinement stage. We obtain $m_i \approx m_i^{\text{target}}$, and all magnetic moments satisfy the required criteria for MaxAE and MAE.

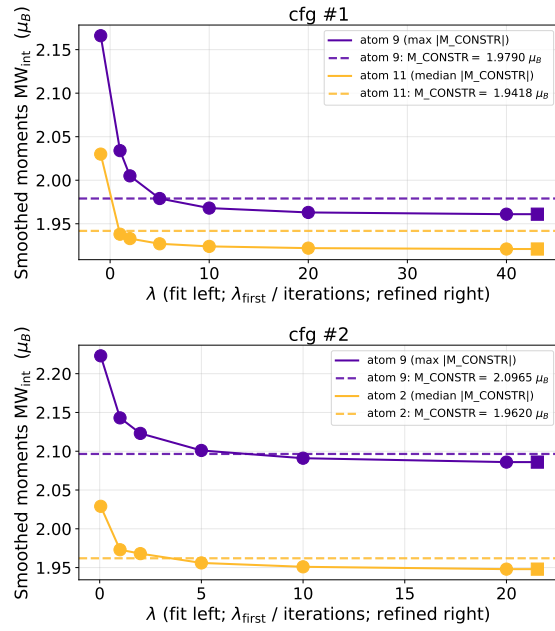


Figure S9: Smoothed magnetic moments m_i^{WS} (reported in OSZICAR) at various stages of the workflow, illustrated with solid lines: the fitting stage, the series of soft-constrained calculations with increasing penalty weight λ , and the refinement stage. Dashed lines show the constraining magnetic moments m_i^{constr} (M_{CONSTR}). The purple solid line corresponds to the maximum absolute target moment, and the yellow solid line to the median of the absolute values over all target moments. Squares denote the results from the refinement stage, while circles correspond to the other stages. We show results for two randomly selected configurations: (top) the first configuration and (bottom) the second configuration.

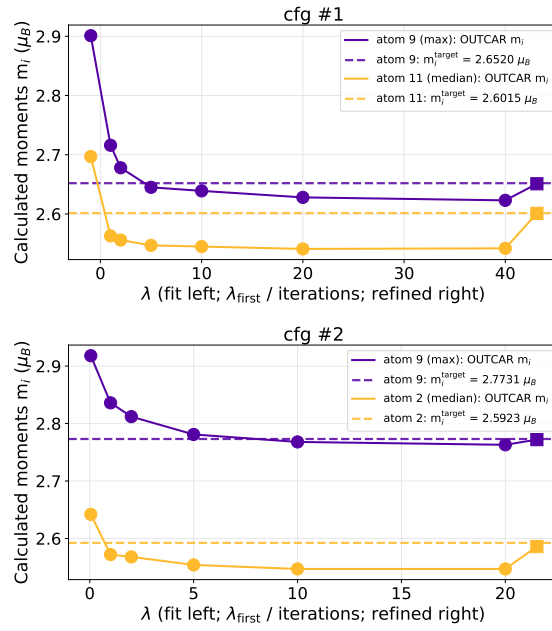


Figure S10: Calculated magnetic moments m_i (reported in OUTCAR) at various stages of the workflow, illustrated with solid lines: the fitting stage, the series of soft-constrained calculations with increasing penalty weight λ , and the refinement stage. Dashed lines show the target magnetic moments m_i^{target} . The purple solid line corresponds to the maximum absolute target moment, and the yellow solid line to the median of the absolute values over all target moments. Squares denote the results from the refinement stage, while circles correspond to the other stages. We show results for two randomly selected configurations: (top) the first configuration and (bottom) the second configuration.

S2. Examples of VASP input files

Below, we provide examples of INCAR files for both unconstrained and constrained DFT calculations in VASP, which we used for Fe-Pd.

Example 1. INCAR file for the unconstrained DFT calculations (LNONCOLLINEAR = .FALSE., LAMBDA=0).

```
SYSTEM = equilibrium non-constrained FePd calculations
ALGO = Normal
EDIFF = 1e-06
ENCUT = 500
IBRION = 1
ICHARG = 2
ISMEAR = 1
ISPIN = 2
ISTART = 0
ISYM = 0
KGAMMA = .TRUE.
LCHARG = .TRUE.
LORBIT = 11
LSCALU = .FALSE.
LWAVE = .TRUE.
NBANDS = 300
NELM = 200
NELMIN = 4
NSW = 0
NPAR = 1
PREC = Accurate
SIGMA = 0.1
RWIGS = 1.404 1.302
```

Example 2. INCAR file for the soft-constrained DFT calculations (LNONCOLLINEAR = .TRUE., LAMBDA>0).

```
SYSTEM = non-equilibrium soft-constrained FePd calculations
ALGO = Normal
EDIFF = 1e-05
ENCUT = 500
IBRION = 1
ICHARG = 1
ISMEAR = 1
ISPIN = 2
ISTART = 1
ISYM = 0
I_CONSTRAINED_M = 2
KGAMMA = .TRUE.
LAMBDA = 0.01
LCHARG = .TRUE
LNONCOLLINEAR = .TRUE.
LORBIT = 11
LSCALU = .FALSE.
LWAVE = .TRUE.
MAGMOM = 2.211 0 0 2.064 0 0 2.260 0 0 2.250 0 0 2.280 0 0 2.162 0 0 2.142 0 0 2.151 0 0 2.345 0 0
2.216 0 0 2.286 0 0 2.261 0 0 2.087 0 0 2.294 0 0 2.220 0 0 2.233 0 0 2.220 0 0 2.195 0 0 2.296 0 0
2.137 0 0 2.245 0 0 2.222 0 0 0.247 0 0 0.238 0 0 0.233 0 0 0.223 0 0 0.231 0 0 0.222 0 0 0.247 0 0
0.225 0 0 0.245 0 0 0.240 0 0
M_CONSTR = 2.211 0 0 2.064 0 0 2.260 0 0 2.250 0 0 2.280 0 0 2.162 0 0 2.142 0 0 2.151 0 0 2.345 0 0
2.216 0 0 2.286 0 0 2.261 0 0 2.087 0 0 2.294 0 0 2.220 0 0 2.233 0 0 2.220 0 0 2.195 0 0 2.296 0 0
2.137 0 0 2.245 0 0 2.222 0 0 0.247 0 0 0.238 0 0 0.233 0 0 0.223 0 0 0.231 0 0 0.222 0 0 0.247 0 0
0.225 0 0 0.245 0 0 0.240 0 0
NBANDS = 850
NELM = 200
NELMIN = 4
NSW = 0
NPAR = 1
PREC = Accurate
SIGMA = 0.1
RWIGS = 1.404 1.302
```